International Journal of Computer Vision and Signal Processing, 14(1), 18-25(2024)

Automated Fracture Detection from Pelvic X-ray: The Impact of Appropriate Labeling on the Performance of Deep Convolutional Neural Network

Rashedur Rahman*

Graduate school of engineering
University of Hyogo

Naomi Yagi

Advanced Medical Engineering Research Institute
University of Hyogo

Keigo Hayashi, Akihiro Maruo, Hirotsugu Muratsu

Hyogo Prefectural Harima-Himeji General Medical Center

Sayoji Kobashi

Graduate school of engineering
University of Hyogo

Abstract

Pelvic X-rays (PXRs) are essential diagnostic tools used to visualize the pelvic region and assess pelvic fractures. The rising incidence of pelvic fractures leads to increased radiologist workload and initial misdiagnoses. As a result, there is a growing need for automated tools to assist doctors in pelvic fracture detection. Artificial intelligence has advanced recently, resulting in several methods for diagnosing PXRs for fractures. However, concerns regarding annotation accuracy and the limitations of PXRs due to constrained viewing angles persist. Some fractures are only visible in 3D computed tomography (CT) images, and it is difficult to understand their visibility in PXR. This study proposes a method for using annotations from pelvic CT to label PXRs, focusing on fracture visibility. Additionally, the impact of labeling PXRs based on visibility to fracture detection performance in PXR images is examined. First, all fractures in CT images are annotated using a 3D surface annotation approach. Next, annotated pseudo PXRs are synthesized from CT images utilizing digitally reconstructed radiographs (DRRs). The annotated pseudo PXRs serve as references for accurately labeling fractures in corresponding PXRs. By training a Resnet-101-based deep convolutional neural network (DCNN) with the labeled datasets considering fracture visibility, the proposed method significantly improved fracture detection performance, achieving an Area Under the Receiver Operating Characteristic (AUROC) of 0.9114. The AUROC of the conventional annotation method was 0.8202.

Contribution of the Paper: This study proposes an innovative method to utilize pelvic CT annotations to improve PXR labeling and enhance the performance of DCNN for fracture detection.

Keywords: Pelvic X-rays, Digitally Reconstructed Radiograph, Pseudo PXR, Pelvic fracture detection

IJCVSP

ISSN: 2186-1390 (Online)
http://cennser.org/IJCVSP

Article History:
Received: 6 December 2023
Revised: 21 January 2024
Accepted: 30 January 2024
Published Online: 5 February 2024

1. Introduction

PXRs are radiographic images of the pelvic region, primarily utilized to provide visualizations of the pelvis and its surrounding anatomical structures. These images serve as a crucial diagnostic tool in the assessment of pelvic fractures. While previous studies have demonstrated that computed tomography (CT) offers enhanced sensitivity and specificity in the detection of pelvic fractures, the diagnostic process typically commences with a PXR examination [1, 2]. Nonetheless, a significant challenge associated with PXR examinations is the growing incidence of pelvic fractures, particularly among elderly patients in various regions [3, 4] including United States [5], Bangladesh [6], Japan [7], Finland [8], and Germany [9]. This surge in patient cases places a considerable burden on radiologists and contributes to initial misdiagnoses [10]. Consequently, there is an increasing demand for automatic tools designed to aid physicians in pelvic fracture detection.

Pelvic region has a complex structure that includes pelvic ring area, hip, acetabulum, and a part of femur. With the advancement in the artificial intelligence field, several methods were proposed to diagnose and detect fractures in PXRs. To avoid complexity, most of the proposed methods focused on diagnosing fractures in specific regions of the PXR. Mawatari et al. assessed the performance of deep convolutional neural networks (DCNNs) based on the GoogLeNet architecture for hip fracture detection in PXR images and compared it with seven radiologists [11]. Their study utilized CT and magnetic resonance imaging (MRI) as the gold standard for annotation and revealed that the radiologists' performance improved with the aid of DCNN. In a multicenter study, Sato et al. demonstrated that a computer-aided diagnosis system based on deep learning improved the diagnostic accuracy of residents in hip fracture detection [12]. This system utilized the Efficient-NetB4 deep learning model, achieving an impressive Area Under Curve (AUC) of 0.99. Similarly, Mutasa et al. proposed a method for detecting and classifying femoral neck fractures using a customized residual connection-based DCNN, achieving AUCs of 0.92 for two-class classification and 0.96 for three-class classification [13]. Beyaz et al. introduced a methodology that combined deep learning with genetic algorithms for femoral neck fracture detection in PXR images [14], additionally exploring the impact of region of interest (ROI) size on deep learning performance, with the highest accuracy of 83% attained for an ROI size of 50×50 pixels. All of these methods required manual cropping of ROIs from the PXR images, hence, making those methods inconvenient for practical implementation.

Other methods were proposed to automate the extraction of ROIs from PXR images before fracture diagnosis. For example, Murphy et al. proposed a two-step method involving the extraction of hip joints from a PXR image in the first step and the subsequent classification of the extracted hip joints for fractures in the second step, utilizing separate convolutional neural networks (CNN) in each of these steps, ultimately achieving a 92% accuracy in hip fracture classification [15]. Krogue et al. introduced a two-step method that combined a single-shot detector for hip region detection with a DenseNet-169 DCNN for fracture classification in PXRs, yielding binary classification accuracy of 93.7% and multi-class classification accuracy of 90.8% [16].

Several other methods used full PXRs to detect fractures in PXRs. Cheng et al. proposed a method based on DenseNet-121 for detecting and visualizing hip fractures in PXRs, achieving an accuracy of 91% with 98% sensitivity after training the model on 25,505 limb radiographs and fine-tuning the model with 3,605 PXRs [17]. Mu et al. developed a femoral neck fracture detection method based on the multi-domain fracture detection network (MFDN), achieving impressive AUCs in internal and external test sets [18]. Twinprai et al. introduced a method based on YOLOv4-tiny for detecting and classifying different hip fractures, obtaining a sensitivity of 96.2% and an accuracy of 95% [19]. Lee et al. employed a meta-learned DCNN that incorporated radiography reports and PXR images for classifying different femur fractures, achieving an accuracy of 86.78% with an F1 score of 0.867 [20]. Kitamura proposed a deep learning-based method capable of diagnosing multiple types of fractures and hardware locations in PXR images, achieving high AUC values [21]. Cheng et al. introduced PelviXNet, a scalable deep learning algorithm combining a feature pyramid network (FPN) and DenseNet-169, trained using weakly supervised point-annotated PXR images, yielding an AUROC of 0.973 on a clinical population test set [22].

While some of the existing studies have illustrated that deep learning can significantly improve the performance of residents in diagnosing fractures from PXR images [11, 12, 15, 18, 19, 22], some studies have suggested the use of alternative medical imaging modalities for different types of fracture detection [2, 3, 23, 24]. Hence, concerns regarding the accuracy of annotations of the existing methods have arisen. Another one of the major challenges in PXR examinations is the restricted viewing angle, which can make some fractures invisible [1]. As a result, the performance of fracture detection methods proposed in existing studies becomes limited. In the study of Mawatari et al. [11], CT and MRI were considered as the gold standard for confirming the presence of fractures in PXR images, although the implications of employing CT and MRI as the gold standard were not extensively discussed.

To address the limitation of the annotation and the resulting influence on existing methods, our study introduces an innovative labeling method. This method introduces the transfer of annotations from pelvic CT to PXRs for fracture detection, taking into consideration the visibility

*Corresponding author
Email addresses: rashed.rahman@ieee.org (Rashedur Rahman), kobashi@eng.u-hyogo.ac.jp (Sayoji Kobashi)

of fractures in PXRs. In the proposed approach, CT images are initially annotated following a 3-dimensional (3D) surface annotation method [25]. After that, digitally reconstructed radiographs (DRRs) are generated from the CT images and their corresponding fracture images to create annotated pseudo PXRs. These pseudo PXRs are used as references to enhance the labeling of PXRs based on the visibility of fractures. A Resnet-101-based DCNN [26], a commonly used residual learning model, is trained and evaluated for PXR detection for various datasets, each constructed with consideration of fracture visibility. The results demonstrate that the proposed annotation method significantly improves the performance of the DCNN.

2. Subjects and Materials

The data used in this study were collected from a total of 477 subjects with a mean age of 66.1 years and a standard deviation of 18.9 years. The range of age was from 20 to 93 years. Among the subjects, 267 were male and 209 were female. The gender information of 1 subject was lost during data anonymization. Among the total subjects, 473 underwent CT examination, with 201 individuals exhibiting signs of pelvic fractures. The CT images were acquired using multidetector-row CT (MDCT) scanners, employing a tube voltage of 120 kVp and automated mAs settings. Additionally, a total of 481 PXRs were obtained from 315 subjects who underwent CT examination. Among these PXRs, 365 images collected from 199 subjects had fractures. The PXRs with implants and missing pelvic regions were excluded from this study. 318 PXRs were considered for this study after the exclusions and the corresponding CTs were used for annotation. Among these 318 PXRs, 246 PXRs had fractures and 72 PXRs were normal without any fracture. All the data were obtained at Steel Memorial Hirohata Hospital in Japan between April 2013 and August 2019. The existence of fractures in 3D-CT and PXR images were confirmed by expert orthopedians in Steel Memorial Hirohata Hospital, Japan.

3. Method

3.1. Data labeling and dataset distribution

In the conventional labeling method, experienced physicians label the PXRs based on the fractures that are only visible in PXRs. However, some fractures may not be visible in PXRs and can only be seen in CT because of the flexibility in the viewing angles and numerous images. Hence, taking CT as reference improves the labeling. For interpreting fractures from CT to PXR based on visibility, a new method of labeling PXR is introduced based on our previous work on CT [25]. The overview of the proposed labeling method is shown in Figure 1. The proposed labeling method can be described in 3 main steps: CT annotation with 3D bone surface annotation, synthesizing annotated pseudo PXR from CT, and PXR labeling and dataset distribution. The improved labeling method is described in the following subsections.

3.1.1. 3D bone surface annotation and CT annotation

The volume of images within a CT dataset is considerable, making manual annotation procedures for identifying fracture areas a challenging and time-consuming task. In order to enhance the efficiency of fracture annotation, this research utilizes the 3D annotation method introduced by Ukai et al. [25], which employs 3D surface rendering techniques. The process of 3D surface rendering involves the representation of the pelvic bone surface within CT images through the utilization of a series of small polygons. Segmentation of the pelvic bone region is accomplished through image processing methods such as thresholding and morphological operations. An annotator selects 3 to 4 adjacent polygons surrounding the identified fractures. The 3D polygons on the 3D bone surface data are annotated by experienced radiologists and doctors. The annotated 3D polygons are subsequently transformed into mask CT. The annotated 3D polygons are subsequently transformed into mask CT. Annotated 3D polygons are represented by coordinates. In the mask CT, the voxels with the corresponding coordinates of 3D polygons are represented by 1. The other voxels remain 0.

3.1.2. Synthesizing annotated pseudo PXR from CT

The annotated pseudo PXRs are generated from the CT and their corresponding mask CT by applying DRR [27]. DRR rendering simulates radiographic images by projecting a 3D image onto a 2D plane. By applying DRR, simulated x-rays pass through a reconstructed CT volume, considering the tissues absorption properties. A parallel projection algorithm, as explained by equation (1), is used to synthesize PXR from CT for this study.

$$X_{DRR}(i,j) = \frac{1}{N}\sum_{k=1}^{N} e^{\left(\frac{\delta}{100}\right)\times\left(\frac{X_{CT}(i,j,k)+1024}{1000}\right)} \qquad (1)$$

Where, δ is the absorption coefficient, X_CT(i,j,k) is the CT value in Hounsfield unit (HU), N is the total number of images in the CT, i, j, and k are the row, column, and slice in the CT, respectively, and X_DRR(i,j) is the synthesized value. δ controls the absorption of X-ray as the tissue density increases. The value of $s\delta$ is chosen to be 90 experimentally in this study. By applying equation (1) on CT and corresponding mask CT, annotated pseudo PXRs are synthesized.

3.1.3. PXR labeling and dataset distribution

The PXRs are labeled manually into four categories, 'only visible', 'visible and invisible, ' 'invisible', and 'normal' by taking the corresponding annotated pseudo PXRs as reference. A PXR is categorized as 'only visible' if all fractures in the annotated pseudo PXR are clearly visible

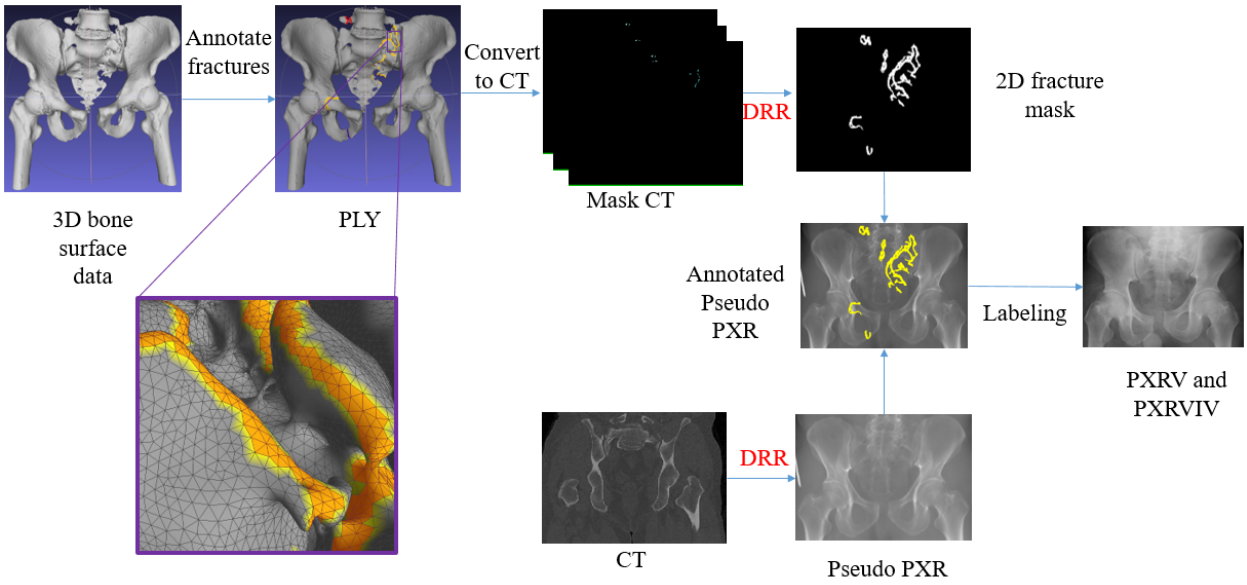

Figure 1: Overview of proposed method for improving the PXR labeling. 3D bone surface data is annotated and converted to mask CT. DRR is applied on the original CT and corresponding mask CT to synthesize annotated pseudo PXR. Original PXR is labeled using annotated pseudo PXR.

in the corresponding PXR. If some fractures are visible while others are not, the PXR is labeled as 'visible and invisible.' If the annotated pseudo PXR indicates a fracture, but the corresponding PXR does not show any visible fracture, it is labeled as 'invisible.' If there is no annotation for a CT, the corresponding PXR is labeled as 'normal.'

Following the proposed labeling method, the PXRs are categorized into two primary datasets, denoted as PXRV and PXRIV. The PXRV dataset includes PXRs labeled as 'only visible' and 'visible and invisible' as the fracture class, alongside 60 normal PXRs. The PXRIV dataset consists of PXRs labeled as 'invisible' in the fracture class, along with 12 normal PXRs. The PXRV dataset is further divided into two datasets, namely PXROV and PXRVIV for the purpose of separate evaluation. The PXROV dataset includes PXRs with 'only visible' labeled as the fracture class and normal PXRs. The PXRVIV dataset comprises PXRs with 'visible and invisible' labeled as the fracture class and normal PXRs. In the conventional labeling method, PXRs are labeled as the fracture class if the fractures are visible in the PXRs. Hence, following the conventional labeling method, PXRs with the 'invisible' label are included in the normal class for comparing the effect of annotation.

3.2. DCNN training

In this study, a residual block-based architecture known as Resnet101 [26] is utilized as the backbone of DCNN. The DCNN consists of residual blocks followed by a global average pooling layer, three fully-connected (FC) layers, a SoftMax (SM) layer and a classification (CL) layer. Rectified Linear Unit (ReLU) is used as the activation function. To address the class imbalance, categorical cross-entropy is used as the loss function with class weights. Class weights are calculated using equations (2) and (3).

$$W_F = \frac{S_{\text{normal}}}{S_{\text{normal}} + S_{\text{fracture}}} \tag{2}$$

$$W_F = \frac{S_{\text{fracture}}}{S_{\text{normal}} + S_{\text{fracture}}} \tag{3}$$

The class weights, WF and WN, represent the class weights of the fracture class and normal class, respectively. Snormal represents the number of normal PXRs, and Sfracture represents the PXRs with fractures. MATLAB 2022b (x64) is used for processing and training on a computer equipped with an AMD Ryzen 7 2700 8-core (3.20 GHz) CPU, 32 GB of DDRAM, and an NVIDIA Titan RTX graphics card.

To ensure uniformity in input data for the DCNN, all images are initially downsampled to dimensions of 224×224. The intensity values are linearly scaled within the range of 0 to 255 also. During the training, the input images are augmented through random rotations, translations, shear transformations, and scaling operations. Furthermore, the DCNN's backbone is pre-trained on the ImageNet dataset [28].

The following re-training process for the DCNN consists of two steps. In the initial step, the FC, SM, and CL layers are trained for 100 epochs with a batch size of 24 and an initial learning rate of 0.000005. Subsequently, the final residual block with the FC, SM, and CL layers, are fine-tuned for an additional 60 epochs, with an initial learning rate of 0.0000001. The batch size remains consistent throughout the training. In both the training and fine-tuning phases, the learning rate is reduced by a factor of 0.1 every 10 epochs.

3.3. Evaluation

3.3.1. Cross-validation

To evaluate the performance of the DCNN for diagnosing PXRs with fractures, a 5-fold cross-validation approach is used for all the datasets. To avoid subject overlap and ensure data separation based on visibility, PXRs are divided into 5 folds, considering subjects and the presence or absence of fractures. Initially, PXRs containing fractures within the PXROV and PXRVIV datasets are individually separated into 5-folds. Later, one fold from PXROV is paired with the same fold from PXRVIV to construct the corresponding fold for PXRV. In parallel, 60 PXRs categorized as normal are similarly distributed into 5-folds. Each set of normal PXRs within a fold is combined with the corresponding fold from PXRV, PXROV, or PXRVIV to create a binary classification problem for fracture detection. The remaining 12 normal PXRs are combined with PXRIV.

3.3.2. Evaluation matrices

To conduct a comparative analysis of a DCNN across PXR datasets divided based on the visibility of fractures, the study utilizes the receiver operating characteristic (ROC) curve and calculates the AUROC. The ROC curve is generated by plotting sensitivities and 1-specificities, with sensitivity and specificity computed from true positive (TP), false positive (FP), true negative (TN), and false negatives (FN). Here, TP signifies correctly identified PXRs with fractures, while FN represents incorrectly identified PXRs with fractures. TN denotes the instances of appropriately identified normal PXRSs, and FN indicates the instances where PXRs with fractures are incorrectly identified as PXR images without fractures. Sensitivity and specificity are calculated using equations (4) and (5).

$$Senistivity = \frac{TP}{TP + FN} \tag{4}$$

$$Specificity = \frac{TN}{TN + FP} \tag{5}$$

The ROC curve is constructed by calculating sensitivities, and 1-specificities, also known as false positive rate (FPR), across varying confidence score thresholds. Finally, AUROC is calculated using equation (6).

$$AUROC = \sum_{i=1}^{n} \text{sensitivity}_{\ i} \times (FPR_i - FPR_{i-1}) \tag{6}$$

4. Result and Discussions

This section presents and discusses the results obtained from the performance evaluation of a DCNN for the detection of pelvic fractures for datasets divided based on visibility of fractures in PXRs. This study primarily focused on comparing the impact of improved labeling with annotated pseudo PXRs with conventional labeling methods. The results are presented in different subsections, each addressing a specific aspect of the study.

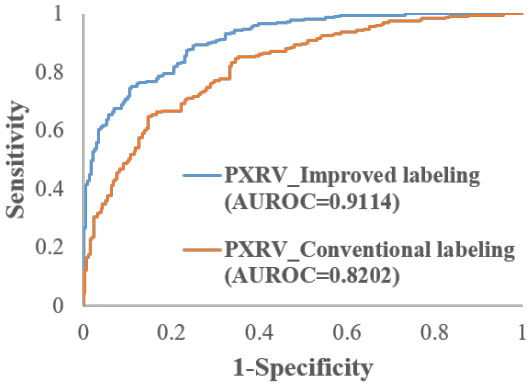

Figure 2: Comparison of ROC for PXRV with improved labeling and conventional labeling.

4.1. Performance evaluation of DCNN for PXRV with proposed labeling and conventional labeling

This subsection assesses the effect of improved labeling with annotated pseudo PXRs on the performance of the DCNN in diagnosing pelvic fractures. The sensitivities and 1-specificities of all the folds were plotted in a single ROC plot and the AUROC were calculated. The combined ROC of PXRV with improved labeling and conventional labeling are shown in Figure 2. The comparison revealed a significant improvement in AUROC, increasing from 0.8202 with conventional labeling to 0.9114 with improved labeling. This indicates that the inclusion of annotated pseudo PXRs to improve the labeling of dataset enhances the model's diagnostic accuracy.

Furthermore, a comparison of sensitivity and specificity at a confidence score threshold of 0.5 was performed. Sensitivity increased from 0.7559 with conventional labeling to 0.7797 with improved labeling. However, the most substantial improvement was observed in specificity, which increased from 0.6747 with conventional labeling to 0.8333 with improved labeling. The specificity improvement was attributed to the exclusion of PXRIV as a fracture class for fracture detection.

Moreover, the study extended its evaluation to PXROV and PXRVIV datasets, revealing that the AUROCs for these datasets also increased significantly after improving the labeling. The comparison of ROCs for PXROV and PXRVIV is shown in Figure 3. This suggests that the benefits of improved labeling extend to various datasets, enhancing the DCNN's performance consistently.

4.2. Performance evaluated of DCNN for PXROV with improved labeling and conventional labeling

This subsection analyzes and compares the DCNN's performance when trained with PXROV, assessing the impact of improved labeling on this specific dataset. The results showed that the AUROC for PXROV increased from 0.7712 with conventional labeling to 0.8377 with improved

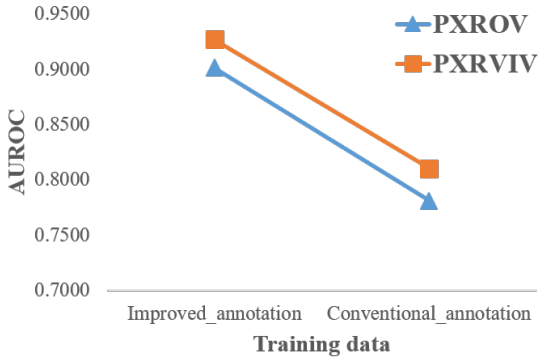

Figure 3: Impact of improved label of PXRV on PXROV and PXRVIV.

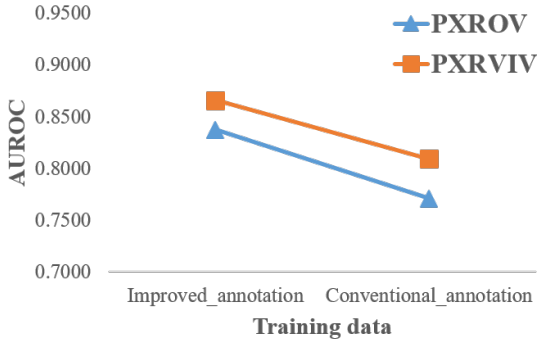

Figure 4: Impact of improved label of PXROV.

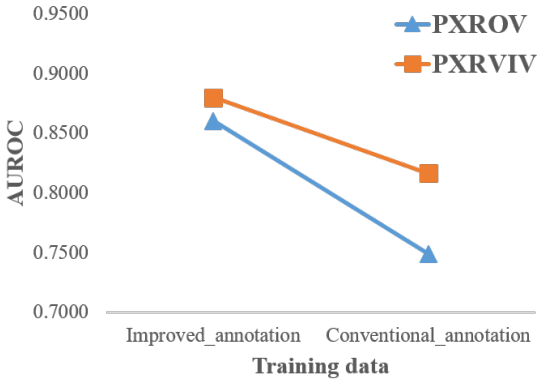

Figure 5: Impact of improved label of PXRVIV.

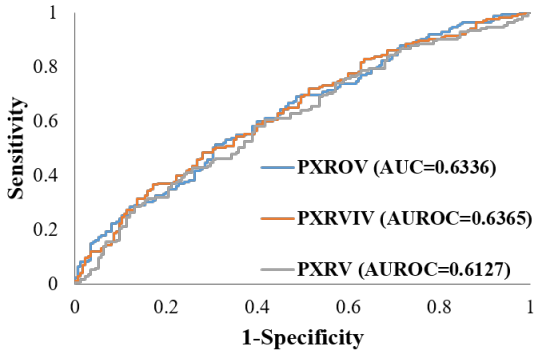

Figure 6: Impact of improved label of PXRIV.

labeling. This improvement highlights the positive influence of the improved labeling method on the DCNN's performance.

Additionally, the DCNN's performance on PXRVIV was evaluated when trained with PXROV, and an improvement in the AUROC was observed, increasing from 0.8096 with conventional labeling to 0.8662 with improved labeling. These results indicate that the advantages of improved labeling extend to cross-dataset performance as well. The comparison of AUROCs for PXROV and PXRVIV is shown in Figure 4.

4.3. Performance evaluation of DCNN for PXRVIV with improved labeling and conventional labeling

This subsection analyzes the performance of the DCNN when trained with PXRVIV, focusing on the impact of improved labeling on this dataset. The results showed an improvement in the AUROC for PXROV, increasing from 0.7488 with conventional labeling to 0.8601 with improved labeling. Similarly, for PXRVIV, the AUROC increased from 0.8163 with conventional labeling to 0.8799 with improved labeling. The comparison is shown in Figure 5. These findings indicate that the improvement in labeling on PXRVIV positively affects the DCNN's performance across different datasets. From Figure 5, it can also be seen that the DCNN performed better to detect PXRVIV than PXROV. This result is expected as the DCNN was trained with PXRVIV.

4.4. Effect of improved label on PXRIV

This subsection explores the impact of improved labeling on PXRIV, a dataset that was excluded from the training of the DCNN in the improved labeling method. The DCNNs trained with PXROV, PXRVIV, and PXRV achieved AUCs of 0.6336, 0.6356, and 0.6127, respectively. The corresponding ROCs are shown in Figure 6. These results suggest that the improved labeling method, while significantly enhancing the performance on other datasets, does not yield substantial improvements for PXRIV. One possible reason is the limited number of invisible fractures in the dataset. Another possible reason might be pretraining the DCNN with the ImageNet dataset. Although ImageNet dataset is widely used to initialize a DCNN, the characteristics of PXR images are significantly different from those of natural images in ImageNet dataset. This observation is critical, as it highlights the limitations of the DCNN trained with data with improved labeling.

5. Conclusion

This study introduces a novel labeling method based on annotated pseudo PXRs to improve the labeling of PXRs.

This study has also provided valuable insights into the importance of improved labeling methods for enhancing the diagnostic performance of a DCNN in the context of pelvic fracture detection from PXRs. By transferring annotations from pelvic CT to label PXRs considering the visibility of fractures, this study shows that the performance of DCNN can be enhanced for pelvic fracture detection. The results also show that improving the labeling approach can enhance the model's specificity greatly, thereby reducing FPs. However, the study also revealed a limitation in the case of the PXRIV which stands for PXR dataset with invisible fractures. Despite the substantial improvements observed in other datasets, the benefits of improved labeling did not extend significantly to PXRIV, highlighting the challenges and limitations of dealing with fractures that are not visible in PXRs. This problem can be addressed by balancing the training dataset for visible and invisible fractures. In future work, there is potential to explore the evaluation of a balanced dataset in terms of fracture visibility and conduct performance comparisons across various DCNN architectures.

Acknowledgment

We express our gratitude to Mahmudul Haque (Independent University, Bangladesh) and Dr. Saadia Binte Alam (Independent University, Bangladesh) for their contributions to formatting and enhancing the language of the manuscript.

Author's Contribution

H.M., S.K., and R.R. designed the experiment. K.H., A.M., and H.M. prepared the data. R.R. conducted the experiment. R.R. and N.Y. analyzed the results. All authors reviewed the manuscript.

References

[1] D. Weishaupt, A. M. Grozaj, J. K. Willmann, J. E. Roos, P. R. Hilfiker, B. Marincek, Traumatic injuries: imaging of abdominal and pelvic injuries, European radiology 12 (2002) 1295–1311.

[2] T. Grieser, Radiological diagnosis of pelvic ring fractures, Der Radiologe 60 (2020) 226–246.

[3] A. Schicho, S. A. Schmidt, K. Seeber, A. Olivier, P. H. Richter, F. Gebhard, Pelvic x-ray misses out on detecting sacral fractures in the elderly–importance of ct imaging in blunt pelvic trauma, Injury 47 (3) (2016) 707–710.

[4] R. Marks, Hip fracture epidemiological trends, outcomes, and risk factors, 1970–2009, International journal of general medicine (2010) 1–17.

[5] E. Michael Lewiecki, N. Wright, J. Curtis, E. Siris, R. Gagel, K. Saag, A. Singer, P. Steven, R. Adler, Hip fracture trends in the united states, 2002 to 2015, Osteoporosis International 29 (3) (2018) 717–722.

[6] A. Hossain, S. Islam, M. F. H. Qasem, S. M. F. Eskander, M. T. Hasan, M. Nahar, Epidemiology of pelvic fractures in adult: our experience at two tertiary care hospital in dhaka, bangladesh, Journal of clinical orthopaedics and trauma 11 (6) (2020) 1162–1167.

[7] H. Hagino, N. Endo, A. Harada, J. Iwamoto, T. Mashiba, S. Mori, S. Ohtori, A. Sakai, J. Takada, T. Yamamoto, Survey of hip fractures in japan: recent trends in prevalence and treatment, Journal of Orthopaedic Science 22 (5) (2017) 909–914.

[8] P. Kannus, J. Parkkari, S. Niemi, H. Sievänen, Low-trauma pelvic fractures in elderly finns in 1970–2013, Calcified tissue international 97 (2015) 577–580.

[9] S. Andrich, B. Haastert, E. Neuhaus, K. Neidert, W. Arend, C. Ohmann, J. Grebe, A. Vogt, P. Jungbluth, G. Rösler, et al., Epidemiology of pelvic fractures in germany: considerably high incidence rates among older people, PLoS One 10 (9) (2015) e0139078.

[10] N. Stec, D. Arje, A. R. Moody, E. A. Krupinski, P. N. Tyrrell, A systematic review of fatigue in radiology: is it a problem?, American Journal of Roentgenology 210 (4) (2018) 799–806.

[11] C.-T. Cheng, T.-Y. Ho, T.-Y. Lee, C.-C. Chang, C.-C. Chou, C.-C. Chen, I. Chung, C.-H. Liao, et al., Application of a deep learning algorithm for detection and visualization of hip fractures on plain pelvic radiographs, European radiology 29 (10) (2019) 5469–5477.

[12] J. D. Krogue, K. V. Cheng, K. M. Hwang, P. Toogood, E. G. Meinberg, E. J. Geiger, M. Zaid, K. C. McGill, R. Patel, J. H. Sohn, et al., Automatic hip fracture identification and functional subclassification with deep learning, Radiology: Artificial Intelligence 2 (2) (2020) e190023.

[13] T. Mawatari, Y. Hayashida, S. Katsuragawa, Y. Yoshimatsu, T. Hamamura, K. Anai, M. Ueno, S. Yamaga, I. Ueda, T. Terasawa, et al., The effect of deep convolutional neural networks on radiologists' performance in the detection of hip fractures on digital pelvic radiographs, European journal of radiology 130 (2020) 109188.

[14] Y. Sato, Y. Takegami, T. Asamoto, Y. Ono, T. Hidetoshi, R. Goto, A. Kitamura, S. Honda, Artificial intelligence improves the accuracy of residents in the diagnosis of hip fractures: a multicenter study, BMC musculoskeletal disorders 22 (1) (2021) 1–10.

[15] S. Mutasa, S. Varada, A. Goel, T. T. Wong, M. J. Rasiej, Advanced deep learning techniques applied to automated femoral neck fracture detection and classification, Journal of Digital Imaging 33 (2020) 1209–1217.

[16] S. Beyaz, K. Açıcı, E. Sümer, Femoral neck fracture detection in x-ray images using deep learning and genetic algorithm approaches, Joint diseases and related surgery 31 (2) (2020) 175.

[17] E. Murphy, B. Ehrhardt, C. L. Gregson, O. von Arx, A. Hartley, M. Whitehouse, M. Thomas, G. Stenhouse, T. Chesser, C. Budd, et al., Machine learning outperforms clinical experts in classification of hip fractures, Scientific Reports 12 (1) (2022) 2058.

[18] L. Mu, T. Qu, D. Dong, X. Li, Y. Pei, Y. Wang, G. Shi, Y. Li, F. He, H. Zhang, Fine-tuned deep convolutional networks for the detection of femoral neck fractures on pelvic radiographs: A multicenter dataset validation, IEEE Access 9 (2021) 78495–78503.

[19] C. Lee, J. Jang, S. Lee, Y. S. Kim, H. J. Jo, Y. Kim, Classification of femur fracture in pelvic x-ray images using meta-learned deep neural network, Scientific reports 10 (1) (2020) 13694.

[20] G. Kitamura, Deep learning evaluation of pelvic radiographs for position, hardware presence, and fracture detection, European journal of radiology 130 (2020) 109139.

[21] C.-T. Cheng, Y. Wang, H.-W. Chen, P.-M. Hsiao, C.-N. Yeh, C.-H. Hsieh, S. Miao, J. Xiao, C.-H. Liao, L. Lu, A scalable physician-level deep learning algorithm detects universal trauma on pelvic radiographs, Nature communications 12 (1) (2021) 1066.

[22] N. Twinprai, A. Boonrod, A. Boonrod, J. Chindaprasirt, W. Sirithanaphol, P. Chindaprasirt, P. Twinprai, Artificial intelligence (ai) vs. human in hip fracture detection, Heliyon 8 (11).

[23] H.-G. Palm, P. Lang, C. Hackenbroch, L. Sailer, B. Friemert, Dual-energy ct as an innovative method for diagnosing fragility fractures of the pelvic ring: a retrospective comparison with mri as the gold standard, Archives of orthopaedic and trauma surgery 140 (2020) 473–480.

[24] I. D. Alexa, B. Veliceasa, O. Alexa, C. Carp, A. Filip, Importance of ct scan in fragility fracture of the pelvis, in: 2020 International Conference on e-Health and Bioengineering (EHB), IEEE, 2020, pp. 1–3.

[25] K. Ukai, R. Rahman, N. Yagi, K. Hayashi, A. Maruo, H. Muratsu, S. Kobashi, Detecting pelvic fracture on 3d-ct using deep convolutional neural networks with multi-orientated slab images, Scientific Reports 11 (1) (2021) 11716.

[26] K. He, X. Zhang, S. Ren, J. Sun, Deep residual learning for image recognition, in: Proceedings of the IEEE conference on computer vision and pattern recognition, 2016, pp. 770–778.

[27] S. Ghafurian, D. N. Metaxas, V. Tan, K. Li, Fast generation of digitally reconstructed radiograph through an efficient preprocessing of ray attenuation values, in: Medical Imaging 2016: Image-Guided Procedures, Robotic Interventions, and Modeling, Vol. 9786, SPIE, 2016, pp. 111–118.

[28] J. Deng, W. Dong, R. Socher, L.-J. Li, K. Li, L. Fei-Fei, Imagenet: A large-scale hierarchical image database, in: 2009 IEEE conference on computer vision and pattern recognition, Ieee, 2009, pp. 248–255.